Theoretical and experimental studies of substitution of cadmium into hydroxyapatite†

J. Terra,*[a] G. B. Gonzalez,[b] A. M. Rossi,[a] J. G. Eon[c] and D. E. Ellis[d]

Received 30th June 2010, Accepted 20th August 2010
DOI: 10.1039/c0cp01032d

Substitution of cadmium into bulk hydroxyapatite $Ca_{(10-x)}Cd_x(PO_4)_6(OH)_2$ (CdHA: $x = 0.12$, 1.3, 2.5) is studied by combining X-ray diffraction data from synchrotron radiation, Fourier transform infra-red spectroscopy (FTIR) and density functional theory (DFT) calculations. Energetic and electronic analyses are carried out for several configurations of Cd substitution for Ca at both cationic sites. Rietveld analysis shows preferential occupation of the Ca2 site by cadmium. FTIR data suggest a non-negligible covalent character of Cd–OH. The much-discussed cation site preference for substitution is determined on the basis of relaxed-lattice energetics, and interpreted in terms of chemical concepts; theory indicates that the Ca2 site is clearly favored and this preference is related to the more covalent character of this site compared to that of site 1.

1. Introduction

Hydroxyapatite (CaHA), $Ca_{10}(PO_4)_6(OH)_2$, is the ideal prototype for the main inorganic phase of bone and teeth.[1] In fact, biological hydroxyapatite is a calcium-deficient, CO_3-containing, non-stoichiometric, disordered apatite. Due to these characteristics and its remarkable ion exchange capability, bone (besides having its obvious supporting function) is also a reservoir of a variety of trace elements. Many of the trace elements are essential for the human body. For example, Zn is one of the most important trace ions necessary for the proper function of over 80 different enzymes,[2] several of them involved in bone metabolism. It is known that Zn^{2+} addition can promote bone formation as well as the trace elements Mn and Cu, which are also required for growth, development and maintenance of healthy bones.[3] However, others such as Pb and Cd have a toxic effect on the human body. These heavy metals have no physiological function and their presence in the human body reflects both Pb and Cd exposures to industrial hazards, harmful food contaminants from the environment and cigarette smoking (in the case of cadmium). Since the body has no mechanism to keep Cd at a safe level, it accumulates in the body. At high levels, Cd toxicity results in severe kidney damage[4] and alters the balance between the rates of bone formation and demineralization as observed in *itai-itai* disease, an epidemic occurrence observed in the Jinzu river basin (Japan) in the 1940s[5] where rice fields were irrigated with highly Cd polluted water. However, there has been a consensus in recent years that even at minimal levels Cd causes an unbalance of the bone turnover mechanism and consequent skeletal demineralization.[5,6] Because of its high ion adsorptivity, CaHA has also been considered and utilized as a material for trapping heavy metals in ground water and soil.[7] In order to understand the Cd–HA interaction in both biological and synthetic CaHA, numerous studies have been focused upon the structural modification induced by Cd in terms of its distribution between the two non-equivalent Ca1 and Ca2 sites available in the CaHA structure.

Structural characterization has been made previously by X-ray diffraction (XRD) in Cd–HA solid solutions synthesized by wet process,[8] hydrothermal methods[9] and from aqueous solutions.[4] Rietveld refinements showed that lattice dimensions decrease linearly with increasing Cd content and that the occupancy of the Ca2 site is slightly favored over Ca1;[8,9] this preference was analyzed in terms of ionic radius and electronegativity of Cd. Tamm and Peld[10] carried out theoretical modeling in fluor- and hydroxyl-apatite where one or two Ca^{2+} per unit cell were replaced with Cd^{2+} and Zn^{2+}. Their results also indicate the Cd energetic preference for Ca2 sites in both singly and doubly substituted CaHA.

In the present work, samples of CaHA were synthesized containing 1.2, 13 and 25 at% Cd by a wet chemical method and characterized by atomic absorption spectroscopy, FTIR and XRD from synchrotron radiation. Based on the XRD refinements several structural model configurations for each Cd concentration were constructed in order to explore physicochemical modifications induced by substitution. Density functional theory (DFT) calculations were then carried out using periodic plane-wave pseudopotential and embedded cluster models on the $Ca_{1-x}Cd_xHA$ solid solutions at low Cd content. These calculations are analyzed in this work in order to verify Cd site preference, and to interpret the lattice response to cation substitution.

2. Materials and experimental methods

Cadmium-doped hydroxyapatite samples, $Ca_{(10-x)}Cd_x(PO_4)_6(OH)_2$ (CdHA: $x = 0.012$, 0.13, and 0.25), were prepared according the following procedure: an aqueous solution containing $Ca(NO_3)_2$ and $Cd(NO_3)_2$ was added dropwise

[a] *Centro Brasileiro de Pesquisas Fisicas, Rio de Janeiro, RJ, Brazil. E-mail: joice@cbpf.br*
[b] *Department of Physics, DePaul University, Chicago, IL, USA*
[c] *Instituto de Química, Universidade Federal do Rio de Janeiro, RJ, Brazil*
[d] *Department of Chemistry and Institute for Catalysis in Energy Processes, Northwestern University, Evanston, IL, USA*

† CCDC reference numbers 783220 and 783221. For crystallographic data in CIF or other electronic format see DOI: 10.1039/c0cp01032d

to a $(NH_4)_2HPO_4$ solution at a flow rate of 5 ml min^{-1}, temperature of 90 °C and pH of 10 controlled by NH_4OH addition. After precipitation, the suspension was kept in digestion for 3 h. The precipitate was then separated by filtration and repeatedly washed with boiling deionized water and dried at 100 °C. The dried powder was manually ground and the particles of size <210 nm were separated by sieving. Elemental analyses by atomic absorption spectroscopy were carried out using a Shimadzu AA 6200 spectrophotometer. The vibrational bands present in the samples were obtained with the IRPrestige-21 Series Fourier Transform Infrared Spectrophotometer, in the region of 4000–400 cm^{-1}, using KBr pellets. XRD data were collected in transmission geometry at the ID15B beamline of the European Synchrotron Radiation Facility (ESRF). The incident X-ray energy of 89.52 keV and the instrumental resolution were determined using the LaB6 NIST standard powder (SRM 660a). Debye rings were obtained using a two-dimensional MAR345 image plate with a diameter of 345 mm (2300 × 2300 pixels). Three data sets were collected by placing the sample at 745, 945 and 1145 mm away from the detector. The Debye rings were radially integrated using MatLab. Rietveld analysis was performed simultaneously on the three diffraction patterns with different instrumental resolutions using the FullProf software.

3. Theoretical methodology

Periodic cell and embedded cluster DFT calculations

In the present work, two complementary approaches were used, both developed within the framework of density functional theory (DFT), to investigate the geometrically relaxed solid solution structure of the CaHA/CdHA system. Structural optimizations were obtained *via* the Vienna *ab initio* simulation package VASP, using a periodic supercell model.[11] There, the projector-augmented wave potential and a plane-wave basis set were employed, using the generalized gradient approximation (PAW-GGA) to describe exchange correlation. The Brillouin zone integration was performed using k-point grids of size 2 × 3 × 3 for relaxation of bulk structures and for calculation of total energy. Cell parameters were generated from experimental concentration-dependent XRD data, and atomic positions were relaxed to minimize atomic forces. Convergence was considered to be achieved when all atomic forces were smaller than 0.02 eV $Å^{-1}$. The cohesive energy may be defined as the difference between the total energy per unit cell and the energy of isolated atomic constituents. Fortunately much of the systematic error in total energies due to exchange and correlation approximations cancels out in such calculated differences. To discuss heat of solution and site preference, the excess energy E_x provides a quantitative measure. E_x is defined here in terms of the energy per unit cell of each configuration as

$$E_x = E(Ca_{1-x}Cd_x) - xE(CdHA) - (1 - x)E(CaHA) \quad (1)$$

where x runs between 0 and 1, and lattice energies are normalized per cation site.

Embedded-clusters containing 93 (centered at Ca1/Cd1) and 107 (centered at Ca2/Cd2) atoms in the variational space representing the end-members (CaHA and CdHA) and two doped hydroxyapatite structures were treated by a first-principles real-space Linear Combination of Atomic Orbitals (LCAO) Discrete Variational Method (DVM)[12] based on DFT and the Local Density Approximation (LDA). The cluster approach is a suitable method to accurately determine the local properties and has been successfully used to investigate the non-equivalent cationic and anionic sites present in pure, doped and related compounds of CaHA.[13–16] The local exchange–correlation potential employed was that of Vosko, Wilk, and Nusair.[17] In order to solve the Poisson equation for the Coulomb potential efficiently, a model density was generated by least-square fitting the "true" charge density to a multipolar expansion[18] centered at the cluster nuclei within any desirable level of precision in order to investigate the modification induced at both cationic sites in replacing Ca by Cd. In the present work, angular terms with l = 0,1,2 were used for the central cation and l = 0,1 for the nearest neighbor oxygens. This procedure guarantees that the different covalent character between Ca–O and Cd–O bonds is properly described and their comparison reliable. The local properties were calculated for the central atom of the cluster, since it is less affected by the truncation effects, and its environment best represents that of the solid.

The variational basis functions used were: Cd {4d,5spd}, Ca {3pd,4sp}, P {3spd}, O {2sp}, and H {1s}. The deep-lying atomic orbitals are treated in the "frozen-core" approximation, *i.e.*, the valence basis functions are orthogonalized to the frozen-core basis functions in the first iteration and the orbitals not included in the variational basis are subsequently kept frozen. The external solid is simulated by embedding the cluster in the charge densities of several layers of neighbor atoms. The long-range Coulomb potential of the infinite lattice is included by use of Ewald summations. In a molecular cluster, the Fermi energy E_F is defined as half-way between the Lowest Unoccupied Molecular Orbital (LUMO) and Highest Occupied Molecular Orbital (HOMO), and is consistent with solid-state methodology. For finite clusters embedded in an infinite medium, as is the present case, E_F tends to float with the net charge of the cluster. Nevertheless, all spectroscopic and chemical features are independent of this computational detail. For sake of comparison between similar systems, use of E_F as a common reference point proves to be useful. Alternatively, one could choose to align some defined spectral feature, such as the top of the valence band. This would not alter any conclusion or interpretation.

Mulliken atomic orbital populations, bond orders (BO) or shared charge between Ca, Cd and O and partial densities of states (PDOS) were employed to analyze the chemical bonding features. Since BO are essentially the inner product $C^{\dagger}SC$ between eigenvectors and the LCAO overlap matrix, they can be either positive or negative. Positive values are interpreted as covalent bonding interactions, and negative values take the meaning of covalent antibonding interactions. In general the metal–oxygen interaction is understood as a mixture of ionic and covalent components. Discussion of BO, PDOS, and general features of CaHA bonding and results expected for cation substitution can be found in ref. 13–15.

Crystal structure and cell models

Complete solid solution between calcium hydroxyapatite (CaHA) and cadmium hydroxyapatite (CdHA), $Ca_{10-x}Cd_x(PO_4)_6(OH)_2$ with $0 \leq x \leq 10$, is described in the hexagonal symmetry group $P6_3/m$. Considering the non-equivalent sites at which the Ca, Cd and O atoms are found in this group, the structure of both end-members can be rewritten as $M1_4M2_6[PO1O2O3_2]_6(O_HH)_2$, where M1 and M2 are the fourfold 4(f) and sixfold 6(h) symmetry cation positions. The phosphate PO_4 tetrahedra form basic structural units and are linked by cations at M1 and M2 sites. Both cation sites may be considered as six-fold coordinated to oxygens forming two easily distinguishable geometries as shown in the magnified views of Fig. 1 for the relaxed end-member CaHA: the $Ca1O1_3O2_3$ metaprism and the distorted $Ca2O2O3_4O_H$ octahedron. The six M2 positions are associated with the two hydroxyl groups in the unit cell, where they form two triangles (labeled as Δ and ∇) twisted by 60° relative to each other and centered on and perpendicular to the *c* crystalline axis. Repetition of the [Δ,∇] arrangement along the *c* direction results in the OH-channel. Moreover, the four cations at M1 sites lie on two adjacent columns (labeled as *k* and *l*) parallel to the *c* axis and are distributed throughout the crystal in the ratio of 2 to 1 in relation to the column defined by hydroxyls (see the amplified view in Fig. 1a). Further information about the crystal structure can be found in ref. 13–16.

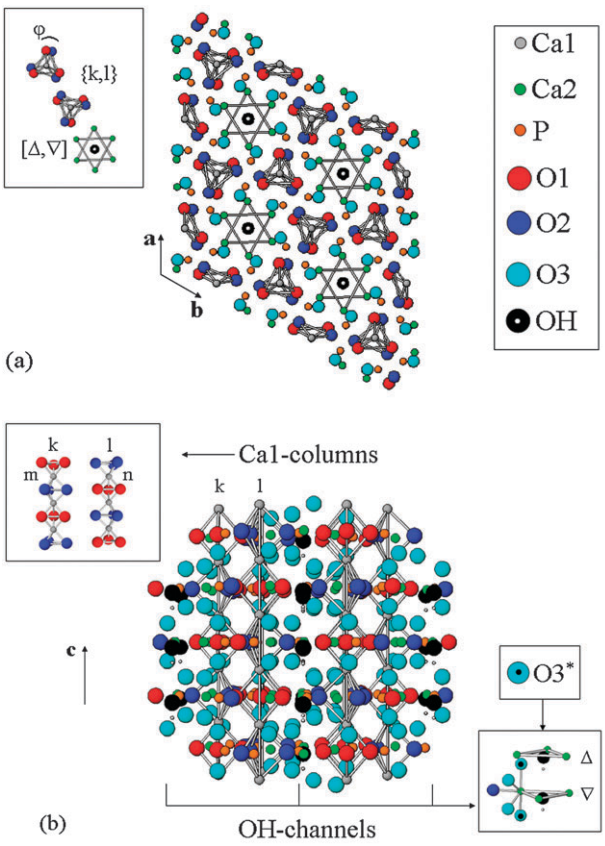

Fig. 1 Calculated pure HA structure: (a) top view; (b) front view. Amplified views of the Ca1 columns: OH-channel arrangement as defined in the text as well as Ca1 adjacent columns (*k*, *l*), and Ca2 adjacent triangles (Δ,∇) with the nearest cation neighbors are also shown.

In order to determine the Cd energetic preference for M1 and M2 sites, at different concentrations, and underlying mechanisms for the preference, the XRD refinement results were used to construct a 2 × 1 × 1 supercell by doubling the CaHA unit cell along the *a* crystalline direction. In view of the prior structural discussion, one concludes that these supercells hold four M1 columns, hereafter identified as {*k*1,*l*1} and {*k*2,*l*2}, and two OH-channels with one [Δ,∇] arrangement in each channel.

The expanded unit cell procedure contains 88 atoms: $Ca_{20-x}Cd_x(PO_4)_{12}(OH)_4$, where $x = 0, 1, 2, 3, 4, 20$ in fact denotes X = 0, 5, 10, 15, 20 and 100 at% solid solution of Cd in CaHA, henceforth identified as CdHA-X. As described above, all atomic positions were allowed to relax, while the unit cell parameters obtained from Rietveld refinements were kept fixed through the relaxation procedure.

The relaxed supercells obtained from the periodic calculations related to the end-members CaHA ($x = 0$) and CdHA ($x = 20$) and those doped with 5 at% ($x = 1$) of Cd in CaHA at both M1 (Cd1HA-5) and M2 (Cd2HA-5) sites were used to construct clusters centered at Ca1, Ca2, Cd1 and Cd2 sites. These sites were surrounded by several atomic coordination shells and the resultant cluster embedded in the charge density of many layers of external potential and charge density as mentioned above.

Supercell configurations

Table 1 shows the supercell configurations modeled for compositions of 5, 10, 15 and 20 at% Cd in the CaHA structure. The second column in the table identifies the substituted sites: for example, the Cd site occupancies identified as '1' and '2' denote substitution of Cd for a single Ca1 and Ca2 respectively, while '12' refers to simultaneous substitution at both Ca1 and Ca2 sites. As introduced in a previous work,[16] two notations were adopted to describe the cationic arrangements related to the 2 × 1 × 1 supercell, as well as to supply information about Cd occupancy throughout the cell. Thus the notation {*k*1(*m*), *l*1(*n*)} {*k*2(*m*), *l*2(*n*)} stands for the Cd occupancy at *k*, *l* Ca1 columns, where *m* and *n* are the numbers of Ca1 intervening between successive Cd. Then, *k*1, *l*1, *k*2, *l*2 labels supply information about Cd1 occupancy along the *a* crystalline axis, while *m* and *n* make known the Cd1 distribution on planes along the *c* crystalline axis. Further information is provided with the SP (same plane) and DP (different plane) labels distinguishing multiple Cd incorporations. On the other hand, the [Δ,∇] notation reports the Cd occupancy at site 2 on one triangle and its adjacent partner along the *c* direction. Moreover, in both cationic notations additional indexes have been included to make available the degree of Cd content found in each configuration so that the comparison among their respective excess energies can be easily made by inspecting Table 1. Thus, labels '*d*', '*i*', and '*c*' identify diluted, intermediate and concentrated content of Cd in CaHA respectively. Occupancies at site 2 have the further

Table 1 Calculated excess energies E_x (meV per cation site) *versus* Cd composition (at%) and configuration at sites 1 and 2. Configurations are ordered by stability with the most stable (lowest E_x) configuration listed first. The Cd occupancy notation is defined in the text

Composition	Cd site Occupancy	Configuration at site 1 {*k*1(m),*l*1(n)} {*k*2(m),*l*2(n)}	Configuration at site 2 [Δ,∇] [Δ,∇]	E_x
5	2	—	[1,0] [Ca2]	−6.4
	1	{1(1), 0(2)} {Ca1}	—	−3.1
10	22-*trans*	—	[1,1]-*trans* [Ca2]	−12.6
	22*d*	—	[1,0] [0,1]	−12.6
	12	{1(1), 0(2)} {Ca1}	[1,0] [Ca2]	−7.7
	11	{1(1), 1(1)} : SP {Ca1}	—	−3.9
15	222d	—	[1,1]-*trans* [1,0]	−16.0
	222-*mer*	—	[2,1]-*mer* [Ca2]	−15.4
	222*c*	—	[3,0] [Ca2]	−11.3
	122-*trans*	{1(1), 0(2)} {Ca1}	[1,1]-*trans* [Ca2]	−14.7
	122*d*	{1(1), 0(2)} {Ca1}	[1,0] [1,0]	−14.3
	112*d*	{1(1), 0(2)} {1(1),0(2)}	[1,0] [Ca2]	−5.8
	112*c*	{2(0), 0(2)} {Ca1}	[1,0] [Ca2]	+0.6
	111*d*	{1(1), 1(1)} : DP {1(1),0(2)}	—	−4.9
	111*c*	{1(1), 2(0)} {Ca1}	—	+3.2
20	2222*i*	—	[2,1]-*fac* [1,0]	−21.8
	2222*d*	—	[1,1]-*trans* [1,1]-*trans*	−19.8
	2222-*trans*	—	[2,2]-*trans* [Ca2]	−18.3
	2222*c*	—	[3,1] [Ca2]	−15.1
	1222	{1(1), 0(2)} {Ca1}	[1,0] [1,1]-*cis*	−16.6
	1122	{1(1), 1(1)} : SP {Ca1}	[1,1]-*trans* [Ca2]	−13.4
	1111*d*	{1(1), 1(1)} : DP {1(1), 1(1)} : DP	—	−4.0
	1111*c*	{2(0), 2(0)} {Ca1}	—	+15.5

indices *–cis vs. –trans* and *–fac vs. –mer* associated respectively with an even and odd number of Cd2 substitutions.[15] They are required to classify the orientation of multiple Cd2 sites on one triangle relative to another. Furthermore, considering that the Cd2–Cd2 distances at a *trans* arrangement are larger than at a *cis* arrangement while the Cd2–Cd2 distances are larger for *mer* than for *fac* geometry, such indices can provide information about the stress at site 2 caused by replacing Ca by Cd. These indices identify configurations which present the *trans*, *cis*, *mer* and *fac* arrangements in one of the two OH channels available in the supercells, otherwise the indices *d*, *i*, or *c* are used. As examples, consider the configurations 2222-*trans* and 2222*d*. The first is identified as [2, 2]-*trans* [Ca2], indicating that all Cd2 are positioned at two adjacent Ca2 triangles, *i.e.*, they belong to the same OH channel, and are arranged in a *trans* geometry. On the other hand, the label *d* adopted for the second configuration is due to the presence of two Cd2 *trans* sets at both OH channels and the fact that the Cd2–Cd2 distance in such orientation is the largest possible for two Cds at a [Δ,∇] set. As expected, mixed substitutions such as the '12' configuration are described by combining the site1 : site2 descriptors and follows the same rules defined for single sites.

This precise notation, with its capability of describing small structural differences among various compositions, may seem needlessly complex. However, in view of many years of literature speculation and only partially successful attempts to correlate the site preference and binding strength of different cation substituents in the CaHA lattice with simple parameters such as ionic radius and electronegativity, it seems clear that an atomic-scale bond- and electronic-structure-based analysis is required. We shall see that the geometric-structure-based empirical models, invoking features such as the twist angle and the *c*-axis chains, are reproduced successfully by theoretical calculations.

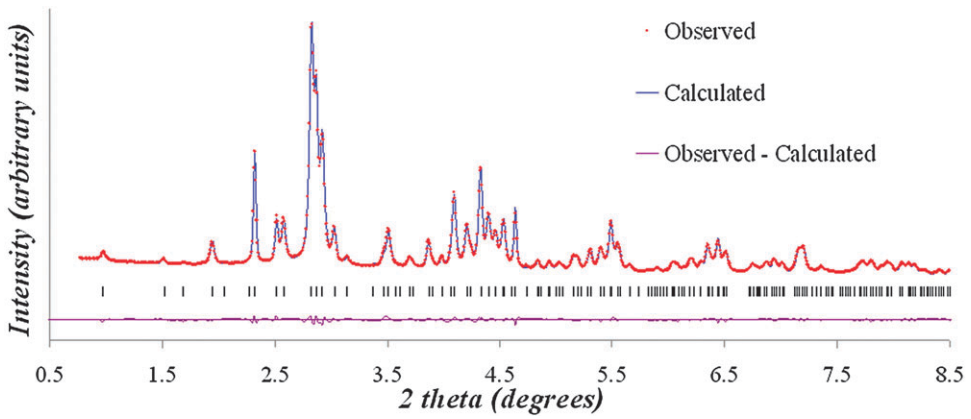

Fig. 2 Experimental and simulated XRD patterns of hydroxyapatite doped with 25 at% Cd.

4. Results and discussion

X-ray diffraction and FTIR

CdHA samples presented X-ray diffraction patterns of crystalline apatite structures; no additional peaks from other mineral phases besides hydroxyapatite were detected. The experimental XRD pattern for sample CdHA-25 and the calculated pattern from Rietveld analysis are shown in Fig. 2 while Fig. 3 and Tables 2 and 3 present the values for lattice parameters, crystallite mean size along [002] and [030] apatite directions and Cd atomic occupancy.† The total cadmium concentrations estimated from Rietveld refinements for each sample were very close to those measured by chemical analyses. The $a = b$ and c cell parameters decreased with increasing Cd content, but contraction of the c axis was more marked in the range of $13 < X < 25$ at%; the data are in agreement with those reported in ref. 19. The particle mean size along c direction (XRD (002) reflection) was larger than in perpendicular directions (XRD (030) reflection), indicating a clear preferential crystallization along that direction. The data suggest that the particle mean size along the [002] direction decreases with cadmium substitution whereas it remained practically constant along the [030] direction. This result shows that preference for crystallization along the c direction is disturbed by cadmium substitution. For small Cd concentrations (1.2 at%) the XRD intensities change only by a very small amount, therefore the uncertainty in the cadmium occupancy is large. Within experimental error, there seems to be no preference for cadmium occupancy into Ca1 and Ca2 sites for this sample. For higher Cd concentrations (13 and 25 at%) the Rietveld refinements revealed a clear preference for Ca2 sites. However, the Cd2/Cd1 occupancy ratio did not change when cadmium substitution increased from 13 to 25 at%.

FTIR spectra of the samples (not shown) presented the characteristic absorption bands due to phosphate and hydroxyl groups in the apatite structure. No significant change in the position of the phosphate bands was registered as Cd substitution increases up to 25 at%. However, in agreement with reported data,[19] cadmium substitution induced a strong shift of the internal OH stretching band, from ν_s(OH) = 3571 cm^{-1} (1.2 at%) to 3564 cm^{-1} (13 at%) and 3555 cm^{-1} (25 at%). Widening of this band suggests local disorder at the OH site. Shift of the librational OH band was also observed from ν_l(OH) = 634 cm^{-1} (1.2 at%) to 628 cm^{-1} (13 at%), accompanied with a strong decrease in intensity, probably explaining why this band is not clearly detected at higher Cd concentration (25 at%). It is known that Sr and Ba substitutions for Ca in hydroxyapatite provoke a shift of ν_s(OH) to higher frequencies,[20] which was associated with lattice expansion within the alkaline-earth series. In contrast, Pb substitution yields a shift to lower frequencies.[21,22] Andres-Verges *et al.*[22] reported a shift from 3573 cm^{-1} to 3560 cm^{-1} in the range $0 < X < 60$ Pb at% where Pb preferentially fills Ca2 and there is no further variation for higher Pb ($X > 60$) content. Such behavior in Pb-substituted apatites was attributed mainly to covalent Pb2–OH interactions. However, due to lattice expansion in Pb-substituted apatites, an opposite effect is expected to counteract that of cation–oxygen bonding. Hence, large shifts of ν_s(OH) to lower frequencies observed in Cd-substituted apatites, combined with XRD refinement data showing partial filling of Ca2 site by Cd, suggest significant covalent bonding between Cd and OH. In this case, the relatively small lattice contraction effect does not mask that of cation–oxygen bonding, producing a drastic shift of the OH stretching band. It should be noted that covalent interactions between Cd and PO_4 groups in cadmium apatites were already considered in ref. 23 to explain the splitting features of degenerate PO_4 bands.

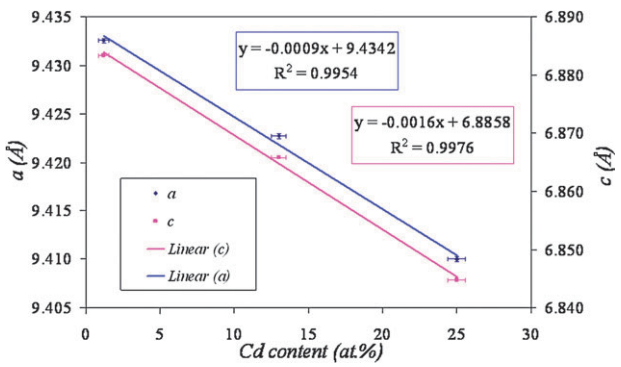

Fig. 3 Lattice parameters *versus* cadmium atomic percent (at%) obtained from atomic absorption.

Table 2 Experimental lattice parameters a, c and Apparent size (Å) for Cd doped hydroxyapatites CdHA-X. Values in parentheses are standard deviations

	X = 1.2%	X = 13%	X = 25%
a	9.4326 (0.0002)	9.4227 (0.0002)	9.4100 (0.0002)
c	6.8833 (0.0002)	6.8659 (0.0002)	6.8448 (0.0002)
Apparent size [002]	516	493	481
Apparent size [030]	152	153	156

Periodic DFT calculations

Using the periodic DFT model, we consider several configurations (Table 1) of the $Cd_xCa_{1-x}HA$ solid solution in the range $0 < x < 0.20$ in order to better understand structure, energetics and occupation of Cd on both cationic Ca1 and Ca2 sites. Let us start by analyzing the metal–oxygen bond distances R_{MO}. Due to the distorted cation environment, a variety of R_{MO} are encountered, which, however, form well-defined subgroups identifiable with end-member compounds.

Pure CaHA and CdHA. The end-members CaHA and CdHA present similar trends for their cation–oxygen bond distances at both M sites, *i.e.*, M1–O1 < –O2 < –O3 and M2–O3* < –O2 < $–O_H$ < –O3 < –O1, where O3* identifies the next-nearest O3 pair (see the amplified view in Fig. 1b) which are bonded to P ions located at planes above and below the M2 plane, while O3 labels the other oxygen bonded to a P ion positioned at the M2 plane. Similarities are also noticed in their cation–cation distances. Bearing in mind that the Cd ionic radius (IR, 0.95 Å) is smaller than that of Ca (0.99 Å), a very slight shortening of the Cd–O and Cd–Cd lengths, compatible with the difference between their IRs of 0.04 Å, is expected if a rigid ion model is applicable. In order to check

Table 3 Total atomic occupancy (at.) of Ca and Cd, as well as the Cd1 and Cd2 atomic and fractional (at%) occupancies at both sites from Rietveld refinements. Values in parentheses are standard deviations

CdHA-X (at%)[a]	Cd (at.)	Ca (at.)	Cd1 (at.)	Cd2 (at.)	Cd1 (at%)	Cd2 (at%)
1.2	0.197 (*0.026*)	9.803 (*0.026*)	0.085 (*0.012*)	0.112 (*0.014*)	2.1 (*0.003*)	1.9 (*0.002*)
13	1.226 (*0.036*)	8.774 (*0.036*)	0.341 (*0.014*)	0.885 (*0.022*)	8.5 (*0.004*)	14.8 (*0.004*)
25	2.349 (*0.048*)	7.651 (*0.048*)	0.678 (*0.016*)	1.671 (*0.032*)	17.0 (*0.004*)	27.9 (*0.005*)

[a] Cadmium concentration measured by atomic absorption.

such a hypothesis, analysis of the end-members is straightforward. Starting with the M1 site, the calculated nearest neighbors Ca1–O1, –O2 bond lengths for CaHA are 2.40 and 2.43 Å respectively, while the distances related to the three O3 second neighbors vary within the interval [2.83, 2.84] Å, which are very close to 2.42, 2.45 and 2.81 Å derived from experimental analysis.[24] For pure CdHA, we have obtained Cd1–O1, –O2 = 2.31, 2.37 Å and Cd1–O3 within the interval [2.88, 2.90] Å, compared to experimental values of 2.33, 2.44 and 2.83 Å.[25] Then, the Cd1–O1, –O2 distances are reduced by 0.09 and 0.06 Å respectively, while Cd1–O3 increases by about 0.06 Å in relation to the corresponding distances of CaHA. At site M2, the six nearest neighbors O3*, O2, O_H and O3 of Ca2 are respectively (2.33, 2.34), 2.34, 2.38 and (2.47, 2.50) Å away from Ca2 in pure CaHA, while the Ca2–O1 distance due to the second neighbor is 2.72 Å. These values are in good agreement with those from experiment: Ca2–O3* = 2.35,2.37, –O2 = 2.36, –O_H = 2.39, –O3 = 2.51, –O1 = 2.70 Å. The corresponding Cd2–O3*, –O2, –O_H, –O3, –O1 bond lengths for CdHA are (2.22, 2.24), 2.34, 2.32, (2.43, 2.49), and 2.68 Å respectively related to experimental values 2.24, 2.34, 2.35, 2.49 and 2.64 Å. At this site, bond length reduction around Cd2 is more uniform than that of Cd1, ranging from 0.00 (–O2) to 0.11 Å (–O3*), indicating a more flexible character for this site. In addition, an inversion of the sequential order of the calculated bond values compared to CaHA takes place, *i.e.* Cd2–O_H < Cd2–O2, while these bond lengths have almost identical values according to experiment. The Cd–O bond lengths discussed above indicate that Cd substitution for Ca is not simply that of rigid divalent ions, and that Cd is somewhat 'softer' which is indicative of significant covalent interactions. The angle defined as the O1–M1–O2 twist angle (φ) projected onto the (001) plane of the $M1O1_3O2_3$ metaprism (Fig. 1a) has been proposed[26–28] as a useful tool for characterizing and comparing apatite compounds. Dong and White also observed an inverse linear relationship between φ and ionic radius of the M1 cation. Thus, since the ionic radius of Cd is smaller that of Ca, pure CdHA must present a shortening of Cd1–O and Cd2–O lengths and these structural modifications can be achieved by increasing φ. We have obtained $\varphi = 22.7^\circ$ and 24.2° for pure CaHA and CdHA respectively, which are close to the experimental values of 23° and 25.8°.

Finally, we observe the relationship between the M2–O3*–P–O3*–M2 chain distance and the *c* lattice parameter as suggested by Mercier *et al.*,[28] *i.e.*, the distances involved in the chain decrease linearly with increasing Cd content.

Site 1 substitution. Initially, consider those configurations in Table 1 related to Cd1 substitutions for Ca1, where a total of 17 Cd1 configurations are represented. Bearing in mind their threefold coordination to O1, O2 and O3 ions, there exist 51 Cd1–O bonds for each Cd1–O1, Cd1–O2, Cd1–O3 set to be analyzed after the relaxation procedure. It is seen that Cd1–O bond lengths lie within the intervals [2.32, 2.43], [2.34, 2.52] and [2.70, 3.10] Å with ranges of (0.12, 0.19, 0.41) Å for –O1, –O2, –O3 respectively. However, scrutiny of these bond lengths shows that about 73% of the –O1 distances fall within [2.32, 2.36] Å, as observed in Fig. 4, which defines a range of only 0.05 Å and an average of 2.34 Å, closely related to both theoretical (2.31 Å) and experimental (2.33 Å) values for pure CdHA. Detailed analysis of –O2 distances reveals in fact two distinguishable intervals [2.34, 2.39] and [2.41, 2.46] containing 65% and 29% of the bond lengths respectively and defining a smaller range of 0.06 Å for both intervals. In this case the average of –O2 distances (2.37 Å) associated with the first interval is identical to that calculated in pure CdHA as discussed above. On the other hand, the average of values within the second interval (2.44 Å) is equal to experiment and equivalent to those, theoretical and experimental, associated with pure CaHA as well. Meanwhile the Cd1–O3 distances lie in a wider interval presenting a more uniform distribution along the range as compared with those distributions due to –O1 and –O2 distances. However, about 47% of them fall within the interval [2.99, 3.03] Å which reduces the range from 0.41 to 0.05 Å. The average of such distances is 3.01 Å, larger than those calculated for both end-members. These results show that the majority of Cd1–O1, –O2 nearest-coordination bonds are weakly affected by the environment and the distances related to them fit with the corresponding distances calculated in CdHA. Deviations from these distances are seen

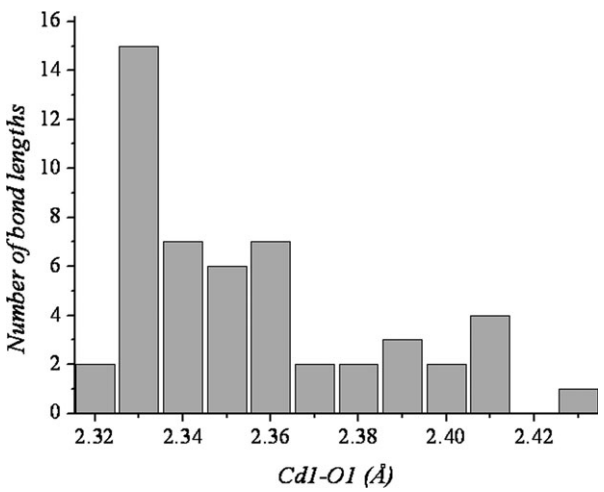

Fig. 4 Histogram of the Cd1–O1 distances for site 1 substitution across the 5–20 at% range.

in configurations such as 111*c* and 1111*c* where the distributions of Cd are concentrated along two Ca1 adjacent columns {*k*, *l*}. On the other hand, the three second neighbors –O3 present significant variation, which is an indication of a weaker bond strength. It is worth mentioning that the majority of the Cd1–O1, –O2 distances are close to that of 2.35 Å found in cubic CdO (a = 4.696 Å) while the twist angle $\varphi \sim 25^\circ$ for the $Cd1O1_3O2_3$ metaprism in the most dilute composition (Cd1HA-5) and ranging from $\sim 23.9^\circ$ to 25.3° for most Cd1HA-20 compositions.

Site 2 substitution. Configurations due to occupancies of site 2 generate thirty Cd2 positions. Keeping in mind that Cd2 is twofold coordinated to both O3* and O3 oxygens, analysis of sixty calculated –O3*, –O3 bond lengths, and thirty from O_H, O2 and O1 coordination has been accomplished. Then, inspection of these distances shows that –O3* bonds lie within the interval [2.29, 2.35], where the distribution of values presents a narrow range of 0.07 Å. The average value of 2.32 Å is close to the corresponding bond in CaHA. On the other hand, the –O3 bond lengths are spread over a wider range of 0.37 Å from 2.37 to 2.73 Å. Nevertheless, 50% of these distances lie within the interval [2.43, 2.49] and 43% within [2.53, 2.62] with ranges of (0.07, 0.1) Å. The first-interval-averaged value of 2.47 Å matches with the calculated –O3 distances in both end-members, while that obtained from the second interval (2.56 Å) is larger than those calculated for CaHA and CdHA. The Cd2–O2, $–O_H$ bond lengths lie within the intervals [2.30, 2.35] and [2.28, 2.45] Å respectively with interval sizes ordered as O2 (0.06) < O_H (0.18) Å. Detailed analysis shows that 80% of the –O2 bond lengths and 83% of the $–O_H$ distances are found within shorter ranges of 0.03 and 0.07 Å associated respectively with the intervals [2.31, 2.33] and [2.28, 2.34] Å. The average distances derived from them are 2.32 (–O2) and 2.31 ($–O_H$) Å, close to those calculated for CdHA (2.34, 2.32 Å). It is worth emphasizing the similarity among the average –O3*, –O2, $–O_H$ bond distances and Cd–O in CdO. Finally, the –O1 bond lengths scatter over a range of 0.13 Å in the interval [2.63, 2.75] Å with 40% and 37% of the values lying within the intervals [2.67, 2.70] and [2.73, 2.74] Å. The average distances associated with them, 2.69 and 2.73 Å, agree with those computed for both end-members CdHA (2.68 Å) and CaHA (2.72 Å). Thus, as observed for the most distant –O3 bonds at site 1, the –O1 distances also exhibit a wider spread as compared to the first neighbors. Here, however, the –O1 bond lengths assume values of both end-members.

Mixed site 1, site 2 substitution. Mixed configurations listed in Table 1 present a total of ten and twelve positions for Cd1 and Cd2 respectively. Analysis confirms the general trends seen above for Cd exclusively sited on either Ca1 or Ca2. However, distributions of Cd1–O distances are strongly modified under mixed substitution: (i) 90% of Cd1–O1, –O2 values are spanned within the intervals [2.33, 2.38], [2.33, 2.43], where the average distances of 2.35 and 2.37 Å related to them are almost identical to the values derived from non-mixed Cd1 substitutions; (ii) 50 and 27% respectively of Cd1–O3 distances are clearly grouped into the intervals [2.95, 3.04], [3.08, 3.14] Å with ranges (0.10, 0.07) Å. The average distance related to the first interval (2.99 Å) is similar to that found with Cd purely at Ca1 sites while the extra interval provide a larger value of 3.12 Å.

Comparison between mixed and pure Cd2 substitution configurations shows that:

(i) The interval of Cd2–O3* bond lengths and its range are identical.

(ii) The range of the two intervals related to –O3 distances increases in the mixed configurations. The average distances obtained are smaller (2.43 Å) and larger (2.65 Å) than those found with Cd purely at Ca2 sites.

(iii) 92% of Cd2–O2, $–O_H$ bond lengths lie within the intervals [2.29, 2.35], [2.27, 2.31] Å with ranges of (0.07, 0.05) Å. The average distances associated are 2.32 and 2.29 Å, which are respectively identical to and a bit shorter than those found in the Cd2HA configurations.

(iv) The two intervals obtained previously for the second neighbor (O1) resolve into a single interval: 92% of the –O1 bond lengths lie within [2.68, 2.75] Å with range of 0.08 Å. The average distance of 2.72 Å is closely related to those computed for the second interval of Cd2HA configurations and pure CaHA.

Excess energies

The excess energies E_x [eqn (1)] of the solid solution $Cd_xCa_{1-x}HA$ structures relative to those of the two end-members are listed in Table 1 and shown graphically in Fig. 5, except for configurations with high Cd1 concentration (labeled by '*c*' in Table 1). Examination of both Table 1 and Fig. 5 shows:

(i) Excess energies always assume negative values for Cd2 occupancies, even for the most concentrated configuration, where all four Cd ions are positioned at two adjacent triangles [Δ,∇]. The values are slightly more negative for those arrangements which maximize the distances between the Cd ions. For example, within the Cd2-15 at% compositions, E_x (222*d*) < E_x (222-*mer*) < E_x (222*c*).

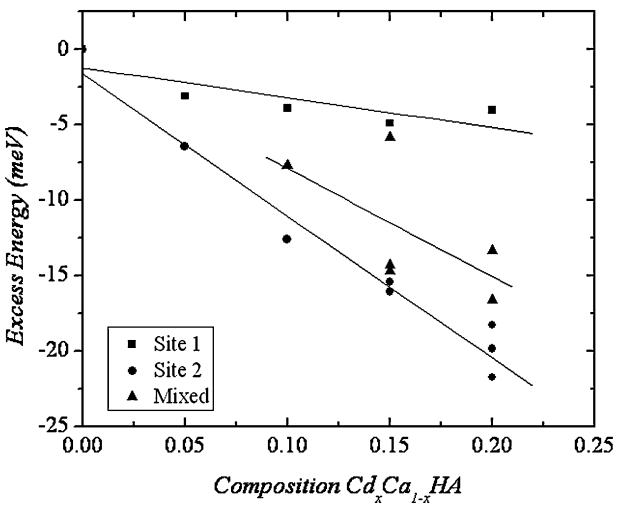

Fig. 5 Excess energy E_x per cation site *versus* Cd composition and neighbor configuration as given in Table 1. Configurations with high Cd1 concentration (labeled by '*c*') in Table 1 are not shown (see text).

(ii) The least favorable values of E_x are due to Cd1 occupancies. These values are positive for the concentrated 111*c* and 1111*c* configurations (not shown in Fig. 5) in which '*c*' means occupancy of Cd1 along two adjacent columns $\{k, l\}$. The effect of such an occupation is remarkable, for example the 1111*d* configuration is about 20 meV more stable than 1111*c*.

(iii) Excess energies obtained from mixed sites reflect the unquestionable preference for site 2 occupation. The more negative values are always associated with configurations with larger Cd2 content. Comparison between the diluted 122*d* and 112*d* configurations shows that the first is about 9 meV more stable than the second. Further, the upper limit for the Cd2–Cd2 distances commented above is observed for 122-*trans* and 122*d* which present comparable E_x values.

Thus, the E_x values are essentially negative across the 0–20 at% range investigated here, except for the 112*c*, 111*c*, and 1111*c* configurations. This trend reveals that the solid solution structures are stable in relation to dissociation into the two end-members CaHA and CdHA at 0 K. At finite temperatures this stability is expected to be enhanced due to a stabilizing configurational free energy term $-T\Delta S$. Within a particular Cd occupancy, stability increases according to site 1 < mixed sites < site 2 demonstrating that occupancy at site 2 is always energetically more favorable than at site 1. Such a preference is clear and already expressed from the lowest Cd content, *i.e.*, the CdHA-5 compositions. Comparison shows that E_x for Cd incorporation at site 1 (−3.1 meV) is about half that of site 2 (−6.4 meV). Besides, it may be noted that the magnitude of E_x increases linearly with Cd content in site 2, while mixed occupancies display a poor linear correlation due essentially to the high E_x value of 112*d* (−5.8 meV) compared to the 122-*trans* and 122*d* configurations (∼−14 meV); a rather weak increase is obtained for site 1 compositions for more diluted structures. First, this means that the energetic gain associated with Cd1 occupancy is lower. Second, closer examination of the graph shows that the Cd2–Cd1 energy difference increases continuously with Cd content. Thus, at the higher Cd content (20 at%), the energetic advantage in adding one more Cd2 is about 5 times larger.

Some comparisons and comments about different cation substitutions in CaHA and proposed mechanisms of site preference follow: comparison of E_x values among $Cd_xCa_{1-x}HA$, $Pb_xCa_{1-x}HA$[15] and $Sr_xCa_{1-x}HA$[16] solid solutions shows that Cd substitution for Ca generates stable solid solutions with respect to the corresponding end-members, causing consequently less stress on the CaHA structure than those found for Sr and Pb incorporations. This result is compatible with a rigid ion model since their ionic radii are ordered as Cd^{2+} (0.95 Å) < Sr^{2+} (1.18 Å) ∼ Pb^{2+} (1.19 Å). However, such a model is insufficient to explain for what reason Cd substitution for Ca2, both experimentally and theoretically, is found to be always preferred as observed for Pb, instead of Ca1 as found for Sr. Identical preferences predicted for both Cd and Pb in CaHA might perhaps be related with their similar electron affinity; *i.e.*, the more covalent character of Cd–O and Pb–O bonds compared to both Ca–O and Sr–O bonds. In fact, data from infrared studies of apatites show that both approaches might be considered. For example, Fowler[20] observed a linear correlation between shifts of the OH vibrational and PO_4^{3-} internal modes and cationic mass or lattice expansion in the calcium–strontium–barium hydroxyapatite sequence. On the other hand, such a correlation is absent in the $Pb_xCa_{1-x}HA$ solid solution[21,22] and related to the more covalent character of Pb compared to the alkaline earths (Ca, Sr, Ba). In addition, these infrared studies demonstrated that the OH vibrational modes are very sensitive to its environment. Considering the fact that OH is coordinated to cations at site 2, shifts associated with OH vibrational modes can provide further information about cationic occupation and the nature of the cation–oxygen bonding at site 2. Our infrared results show an unquestionable decrease in OH stretching modes with increasing of Cd content as reported for Pb-substituted apatites in the range 0 < X < 60 Pb at%,[22] characterizing a predominant role of Cd2–OH interaction. In order to address this question, a detailed electronic structure investigation has been performed on the end-members CaHA, CdHA, cubic CdO, and the Cd1HA-5, Cd2HA-5 solid solutions since the preference for site 2 is already significant at these most dilute compositions.

Embedded cluster DFT calculations

Tables 4 and 5 show the Mulliken-type charges and atomic orbital populations respectively for the M1 and M2 sites obtained from three clusters embedded in CaHA, CdHA-5 and CdHA, where O1, O2, O3*, O3 and O_H are those oxygens lying closer to the central cation. The coordination of these atoms is completely represented within the variational space of the clusters. It is seen that the idealized divalent Ca^{2+} $4s^0$ and Cd^{2+} $4d^{10}$ $5s^0$ configurations in both M1 and M2 sites are augmented by charge transfer from coordinated O ions. The end-members CaHA and CdHA attain almost identical effective charges of 1.87*e* and 1.80*e* at M1 and M2 sites respectively, while in the CdHA-5 clusters, the charge associated with the Cd2 site presents a value slightly less positive (1.85*e*). From the clusters centered at M2 sites we obtain charges of −0.84*e*, −0.83*e* and −0.80*e* for the OH radical. They are reasonably close to the formal charge of −1*e* and their decreasing values from CaHA to CdHA indicate a more covalent cation–OH bond character of Cd than Ca. Mulliken analysis suggests that the M2 site somewhat favors charge transfer from coordinated

Table 4 Self-consistent Mulliken atomic populations and net charges for selected sites in M1-centered clusters in the end-members (HA, CdHA) and doped CdHA-5 at M1 sixfold site

		HA (M1 = Ca)		CdHA-5 (M1 = Cd)	CdHA (M1 = Cd)
M1	3p	5.99	4d	9.99	9.99
	3d	0.09	5s	0.03	0.03
	4s	0.00	5p	0.03	0.03
	4p	0.05	5d	0.08	0.09
	Charge	1.87		1.87	1.86
O1	2s	1.93		1.94	1.94
	2p	5.57		5.59	5.58
	Charge	−1.50		−1.53	−1.52
O2	2s	1.93		1.94	1.94
	2p	5.55		5.56	5.60
	Charge	−1.48		−1.50	−1.54

Table 5 Self-consistent Mulliken atomic populations and net charges for selected sites in M2-centered clusters in the end-members (HA, CdHA) and doped CdHA-5 at M2 sixfold site

		HA (M2 = Ca)		CdHA-5 (M2 = Cd)	CdHA (M2 = Cd)
M2	3p	5.99	4d	9.98	9.98
	3d	0.10	5s	0.03	0.03
	4s	0.02	5p	0.03	0.04
	4p	0.08	5d	0.11	0.15
Charge		1.81		1.85	1.80
O2 2s		1.93		1.93	1.94
2p		5.55		5.56	5.59
Charge		−1.48		−1.49	−1.53
O3* 2s		1.93		1.94	1.94
2p		5.56		5.55	5.57
Charge		−1.49		−1.49	−1.51
O3 2s		1.93		1.93	1.94
2p		5.56		5.57	5.58
Charge		−1.49		−1.50	−1.52
O_H 2s		1.95		1.95	1.96
2p		5.58		5.60	5.61
Charge		−1.53		−1.55	−1.57
H 1s		0.31		0.28	0.23
Charge		0.69		0.72	0.77
OH Charge		−0.84		−0.83	−0.80

O to cation, compared to M1. It is worth noticing that the diffuse Cd 5d virtual orbital accounts for the most significant amount of transferred charge at both cation sites: about three times larger than those computed from the Cd 5s and 5p orbitals. A similar trend is observed in CaHA for the Ca 3d orbital at M1 site; *i.e.*, Ca 3d > 4p > 4s, while at the M2 site Ca2 3d and 4p occupancies are comparable and about four times larger than those obtained for the Ca2 4s orbital. Finally, we obtain a charge of 1.87*e* for Cd of cubic CdO arising from the Cd $4d^{9.99}5s^{0.06}5p^{0.04}5d^{0.04}$ configuration.

Fig. 6 displays the summed BO (off-diagonal charge matrix elements) obtained from the Cd1HA-5, Cd2HA-5 and cubic CdO embedded clusters. We can easily identify the positive covalent bonding character of OH (strong) and of Cd–O (weak) in cubic CdO. This can be contrasted to the negative 'antibonding covalency' of Cd–O at substitution sites in Cd1HA-5 and Cd2HA-5 compositions, representing a small degree of covalent density distributed over six ligands. These BOs range from 0.06 to 0.18*e* in magnitude; the Cd1–O1, O2 BO are comparable, while the Cd2–O bonds present values slightly more negative and ordered in magnitude as Cd2–O2 > –O3* > $–O_H$ > –O3. BOs calculated for pure CdHA are similar to those presented in Fig. 6, while those obtained in pure CaHA range from twice as much negative at site 1 and from 20 to 50% larger at site 2. This result is compatible with the greater electronegativity of Cd. It is worth mentioning that the differences in BOs seen at site 1 are related to the M1–O distances: we observe an inverse relationship between antibonding character of the M1–O interaction and bond lengths. At site 2, such correspondence occurs for the Ca2–O bonds in pure CaHA (not shown). For substituted Cd2HA-5, the BOs are ordered in magnitude as Cd2–O2 > –O3* > $–O_H$ > –O3 while the bond lengths as Cd2–O_H, O2 (2.30 Å) < –O3* (2.34 Å) < O3 (2.47, 2.60 Å). Then the correspondence between BOs and bond lengths is observed, except for the Cd2–O_H bond which presents a shared charge 20% greater than that calculated for Cd2–O2, although O_H is as close as O2 is to Cd. For pure CdHA (not shown), BOs are negative and ordered in magnitude as Cd2–O_H (0.18*e*) > –O2 (0.17*e*) > –O3* (0.15*e*) > –O3 (0.07*e*) and the bond lengths as Cd2–O3* (2.23 Å) < $–O_H$ (2.32 Å) < –O2 (2.34 Å) < –O3 (2.43, 2.49 Å). In this case, Cd2–O_H, –O2 bonds present similar lengths and BOs, while the smallest bond length (Cd2–O3*) retains a shared charge greater than either. Thus, the relationship between BO and distance is established, if the Cd2–O3* bond is excluded. The preceding discussion suggests that Ca1, Cd1–O BOs present similar trends, which is not found in the Cd2–O BOs. Besides, we have observed a continuous and significant increase in the O_H–H bond order with increasing of Cd content: 0.653, 0.714 (shown in Fig. 6), and 0.780 for CaHA, CdHA-5 and CdHA respectively. This result clearly demonstrates the notable sensitivity of OH to local disturbance due to Cd substitution for Ca2. Such sensitivity is also evidenced by the considerable shift of the OH stretching mode in the range 1.2 < X < 25 at% Cd obtained from our FTIR data.

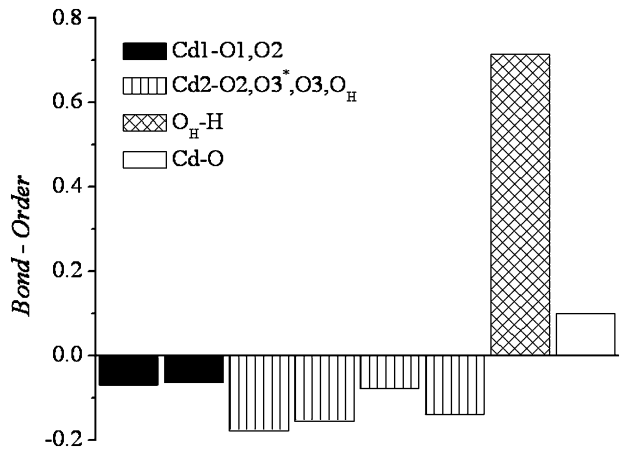

Fig. 6 Calculated bond orders (BO) derived from the Cd1HA-5, Cd2HA-5 and cubic CdO embedded clusters. Labels 1, 2, 3 and the subscript H denote non-equivalent oxygen sites as described in the text.

The partial densities of states (PDOS) for the substituted Cd1, Cd2HA-5 clusters are displayed in Fig. 7. The zero of energy is chosen so that the Fermi level E_F corresponds to 0. The oxygen orbital projections present dissimilarities at both Cd1 (Fig. 7a) and Cd2 (Fig. 7b) sites related to the non-equivalent sites at which O atoms are found. However, such differences seem to be more pronounced among the three O2, O3 and O_H oxygen sites involved with Cd2 coordination than with those (O1, O2) associated with Cd1. This result is compatible with the higher symmetry around Cd1, whose Cd1–O1, –O2 bond lengths are about 2.35 Å and $\varphi \sim 25^\circ$ as discussed above. Then, we can observe in Fig. 7a that for both O1 and O2, the lowest-energy band below E_F, essentially O 2s, ranges from −22 to −17 eV and is partitioned into two peaks with similar profile and considerable overlap between

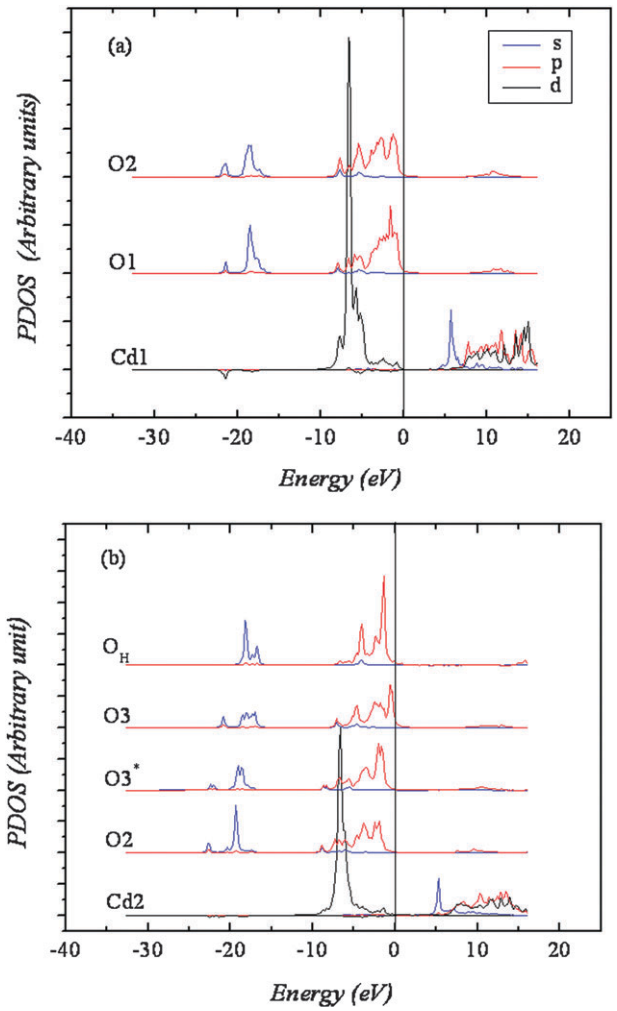

Fig. 7 Partial densities of states (PDOS) for CdHA-5 at both Cd1 (a) and Cd2 (b) sites. The zero of the energy scale is set at the Fermi energy.

them. In contrast, we can notice in Fig. 7b that O2, O3* and O3 2s bands spreading over −23 to −17 eV are represented by distinct distributions, while the O_H 2s band presents an isolated narrower distribution ~3 eV wide. A significant mixture between O3 and O_H is noted and these, to a lesser extent, with O3*, which in turn present notable overlap with the O2 2s band. In common, every O 2s band shown in Fig. 7 presents a small mixture with O 2p. The upper oxygen valence band is separated from the O 2s band by a sizable gap of approximately 8 eV and it is dominated by O 2p levels, as expected in a typical oxide.

Comparison among O 2p bands shows: (i) they are about 8.5 eV wide; (ii) they exhibit considerable overlapping which is more pronounced between O1, O2 in the Cd1HA-5 cluster (Fig. 7a); (iii) the O 2p bands in Cd2HA-5 (Fig. 7b) present more similar profiles compared to those of the Cd1HA-5 cluster. Contributions from O 2s at the bottom of the O 2p band overlap slightly with all O 2p orbitals, and are consistent with formation of sp-bonding hybrid states. The highest-energy valence bands straddling the Fermi level also include the 10 states related to the both Cd1 and Cd2 4d orbitals. We can observe in Fig. 7 that most of these states are concentrated within the peak at −7 eV, which is part of an asymmetric peak structure ranging from −9 to 0 eV. Considering both O 2p and Cd 4d PDOS, we can easily visualize the composition of the cluster valence orbitals (CVO) related to the Cd–O coordination. The CVOs can be divided into three groups according to the degree of mixture between Cd 4d and O 2p orbitals, *i.e.*, at lowest energies the CVOs present small and comparable contributions from both O 2p and Cd 4d; at the intermediate region (from −8 to −5 eV) the major contribution for CVOs is due to the Cd 4d orbitals, while at higher energies the participation of O 2p orbitals becomes dominant. Then, except for O_H 2p orbitals, which show a rather small contribution for the CVOs within the intermediate region of energy, the remaining oxygens present a considerable mixture with Cd over the entire valence energy range. Contributions of Cd 5s, 5p and 5d orbitals are significant within the low-lying excited states, which is compatible with the Mulliken configurations discussed above of Cd1 $5s^{0.03}$ $5p^{0.03}$ $5d^{0.08}$ and Cd2 $5s^{0.03}$ $5p^{0.03}$ $5d^{0.11}$; there, a perfect overlapping between 5p and 5d features characterizes the formation of strongly hybridized states. For comparison, we have calculated the PDOS for CaHA and cubic CdO (not shown). At the lowest-energy region, from −17 eV to −15 eV, the PDOS derived from cubic CdO presents an isolated symmetric narrow peak centered at −16 eV essentially due to the four O 2s states. The upper valence band is formed by a distribution ranging from −9 eV to 0 eV representing the 36 states related to the six O 2p coordinated to Cd and the Cd 4d band represented by an asymmetric distribution ranging from −9 eV to −5 eV; overlap between O 2p and Cd 4d orbitals takes place only at lower energies of the O 2p band. This result is consistent with the positive Cd–O BO values shown in Fig. 6. In contrast with the CdHA-5 PDOS, the low-lying excited states are characterized by a significant mixture between 5s and 5d orbitals and, to a lesser extent, 5p. For both Ca1HA and Ca2HA clusters the lowest-energy bands (from ~−22 eV to −16 eV) are formed by distributions due to O 2s and Ca1 3p states; overlap occurs only near the top of the O 2s band. This result accounts for the more negative BO values derived from pure CaHA as discussed above. The higher-energy valence bands straddling E_F are due to O 2p; contributions from the Ca1, Ca2 4s, 4p and 4d orbitals are found in the low-lying excited states, compatible with their Mulliken populations (Tables 4 and 5) and strongly mixed.

5. Conclusions

X-ray diffraction using a high-intensity synchrotron source and a 2-D detector allowed us to obtain well-defined peaks and accurate analysis of Cd substitution for Ca in hydroxyapatite for low cadmium concentration, to greater precision than possible in previous experiments. Rietveld refinements showed that Ca2 site substitution is clearly favored in 13 and 25 at% Cd. FTIR analyses suggested non-negligible covalent character of Cd–OH bonds.

Formation energies and electronic mechanisms of bonding and cation site preference of $Cd_xCa_{1-x}HA$ solid solutions were investigated using first principles theory. Two complementary methodologies based on the DFT framework,

periodic supercells and embedded clusters, permitted the detailed analysis at the atomic-bond level of the occupation of both cationic sites in the hydroxyapatite structure, using several supercell configurations in the concentration range $0 < X < 20$ at% Cd. Substitution at either Ca1 or Ca2 sites was found to be thermodynamically favorable at almost all concentrations studied; an exception is seen in configurations with Cd1–Cd1 clustering on two Ca1 adjacent columns (positive E_x). The energetic preference for Cd2 occupancies is unquestionable, even for the most concentrated configuration; configurations which maximize the distances between the Cd ions are slightly more favored.

Detailed analysis of cation–oxygen distances showed that most of theoretical Cd–O bond lengths converged to values close to pure CdHA. Comparison between Cd–O and Ca–O bond orders demonstrated that the small negative BOs in both Cd1 and Cd2 sites may be interpreted as evidence of ionic–covalent interaction with weak "antibonding" molecular orbital character, confirming FTIR interpretation. Thus, arguments about site preference, based upon either ionic radius and/or electronegativity, are seen to be inadequate to analyze metal–ligand interactions in CdHA; a more covalent character of site 2 determines its preferential occupation by Cd.

Acknowledgements

Work supported in part by the Supercomputing Center of the Federal University of Rio Grande do Sul and by the US Department of Energy through the Institute for Catalysis in Energy Processes at Northwestern University, Grant no. DE-FG-02-03ER15457. A.M. Rossi and J.-G. Eon thank CNPq (Conselho Nacional de Desenvolvimento e Pesquisa) from Brazil for support. We are grateful for the use of the ID15B beamline at the ESRF facility.

References

1 F. Apfelbaum, I. Mayer and J. D. B. Featherstone, *J. Inorg. Biochem.*, 1990, **38**, 1–8.
2 A. Peretz, T. Papadopoulos, D. WiLtems, A. Hotimsky, N. Michiels, M. Siderova, P. Bergmann and J. Neve, *J. Trace Elem. Med. Biol.*, 2001, **15**, 175–178.
3 J. H. Beattie and A. Avenell, *Nutr. Res. Rev.*, 1992, **5**, 167–188 and references therein.
4 N. C. Blumenthal, V. Cosma, D. Skyler, J. LeGeros and M. Walters, *Calcif. Tissue Int.*, 1995, **56**, 316–322.
5 J. Godt, F. Scheidig, C. Grosse-Siestrup, V. Esche, P. Brandenburg, A. Reich and D. A. Groneberg, *J. Occup. Med. Toxicol.*, 2006, **1**, 22.
6 L. Järup, *Nephrol. Dial. Transplant.*, 2002, **17**, 35; T. Miyahara, Y. Oh-e, E. Takaine and H. Kozuka, *Toxicol. Appl. Pharmacol.*, 1983, **67**, 41–48.
7 H. S. Park, I. T. Kim, H. Y. Kim, K. S. Lee, S. K. Ryu and J. H. Kim, *J. Ind. Eng. Chem.*, 2002, **8**, 318; A. Chartier, C. Meis and J. D. Gale, *Phys. Rev. B: Condens. Matter Mater. Phys.*, 2001, **64**, 085110; C. Meis, J. D. Gale, L. Boyer, J. Carpena and D. Gosset, *J. Phys. Chem. A*, 2000, **104**, 5380.
8 A. Nounah, N. Maroufi, Y. Ait Ichou, J. L. Lacout and J. M. Savariault, *J. Phys. IV*, 2005, **123**, 251–254.
9 K. Zhu, K. Yanagisawa, R. Shimanouchi, A. Onda and K. Kajiyoshi, *J. Eur. Ceram. Soc.*, 2006, **26**, 509–513.
10 T. Tamm and M. Peld, *J. Solid State Chem.*, 2006, **179**, 1581–1587.
11 G. Kresse and J. Hafner, *Phys. Rev. B: Condens. Matter*, 1993, **47**, 558–561; G. Kresse and J. Furthmüller, *Phys. Rev. B: Condens. Matter*, 1996, **54**, 11169–11186; G. Kresse and J. Furthmüller, *Comput. Mater. Sci.*, 1996, **6**, 15–50.
12 D. E. Ellis and D. Guenzburger, *Adv. Quantum Chem.*, 1999, **34**, 51; D. E. Ellis and J. Guo, in *Electronic Density Functional Theory of Molecules, Clusters, and Solids*, ed. D. E. Ellis, Kluwer, Dordrecht, 1995, p. 263; D. E. Ellis, in *Handbook on the Physics and Chemistry of the Actinides*, ed. A. J. Freeman and G. H. Lander, North-Holland, Amsterdam, 1985, p. 1.
13 J. Terra, M. Jiang and D. E. Ellis, *Philos. Mag. A*, 2002, **82**, 2357.
14 M. Jiang, J. Terra, A. M. Rossi, M. A. Morales, E. M. Baggio-Saitovitch and D. E. Ellis, *Phys. Rev. B: Condens. Matter Mater. Phys.*, 2002, **66**, 224107.
15 D. E. Ellis, J. Terra, O. Warschkow, M. Jiang, G. B. González, J. Okasinski, M. J. Bedzyk, A. M. Rossi and J. G. Eon, *Phys. Chem. Chem. Phys.*, 2006, **8**, 967–976.
16 J. Terra, E. R. Dourado, J. G. Eon, D. E. Ellis, G. Gonzales and A. M. Rossi, *Phys. Chem. Chem. Phys.*, 2009, **11**, 568–577.
17 S. H. Vosko, L. Wilk and M. Nusair, *Can. J. Phys.*, 1980, **58**, 1200.
18 B. Delley and D. E. Ellis, *J. Chem. Phys.*, 1982, **76**, 1949.
19 A. Yasukawa, M. Higashijima, K. Kandori and T. Ishikawa, *Colloids Surf., A*, 2005, **268**, 111–117.
20 B. O. Fowler, *Inorg. Chem.*, 1974, **13**, 207–214.
21 A. Bigi, M. Gandolfi, M. Gazzano, A. Ripamonti, N. Roveri and S. A. Thomas, *J. Chem. Soc., Dalton Trans.*, 1991, 2883–2886.
22 M. Andres-Verges, F. J. Higes-Rolando, C. Valenzuela-Calahorro and P. F. Gonzalez-Dias, *Spectrochim. Acta, Part A*, 1983, **39**, 1077–1082.
23 W. E. Klee and G. Engel, *J. Inorg. Nucl. Chem.*, 1970, **32**, 1837.
24 M. I. Kay, R. A. Young and A. S. Posner, *Nature*, 1964, **204**, 1050–1052.
25 M. Hata, K. Okada and S. Iwai, *Acta Crystallogr., Sect. B: Struct. Crystallogr. Cryst. Chem.*, 1978, **34**, 3062–3064.
26 T. J. White and Z. L. Dong, *Acta Crystallogr., Sect. B: Struct. Sci.*, 2003, **59**, 1–16.
27 Z. L. Dong and T. J. White, *Acta Crystallogr., Sect. B: Struct. Sci.*, 2004, **60**, 138–145; Z. L. Dong and T. J. White, *Acta Crystallogr., Sect. B: Struct. Sci.*, 2004, **60**, 146–154.
28 P. H. J. Mercier, Y. Le Page, P. S. Whitfield, L. D. Mitchell, I. J. Davidson and T. J. White, *Acta Crystallogr., Sect. B: Struct. Sci.*, 2005, **61**, 635–655.

